Microprism-based two-photon imaging of the lateral cortex of the mouse inferior colliculus reveals novel organizational principles of the auditory midbrain

Baher A. Ibrahim[1,2], Yoshitaka Shinagawa[1, 2], Gang Xiao[1,2,3], Alexander R. Asilador[2,3,4], & Daniel A. Llano[1,2,3,4,5]

1- Department of Molecular & Integrative Physiology, University of Illinois at Urbana-Champaign, IL, USA.

2- Beckman Institute for Advanced Science & Technology, University of Illinois at Urbana-Champaign, IL, USA.

3- Neuroscience Program, University of Illinois at Urbana-Champaign, IL, USA.

4- School of Molecular & Cell Biology, University of Illinois at Urbana-Champaign, IL, USA.

5- Carle Illinois College of Medicine, University of Illinois at Urbana-Champaign, United States, IL, USA.

Abstract:

The inferior colliculus (IC) is an information processing hub that receives widespread convergent projections. It contains two non-lemniscal divisions - the dorsal (DC) and lateral (LC) cortices - that receive major cortical and multisensory projections. The LC in particular has repeated molecular motifs that govern its input-output relationships. However, because the LC is buried deep within a sulcus, it has been impossible to study by imaging, and thus difficult to answer questions about its functional organization. Here, we couple two-photon microscopy with use of a microprism to reveal the first-ever sagittal views containing functional maps of the LC with cellular resolution. We used this novel approach to examine neuronal responses with respect to LC motifs, and demonstrate the LC is functionally distinct from DC. This method will not only provide new insights about the auditory system, but will also permit imaging of hidden brain regions previously un-imageable by conventional means.

Introduction:

The inferior colliculus (IC) is a critical integration center in the auditory system(Ito & Oliver, 2012). The IC comprises a major lemniscal division, the central nucleus (ICC), that receives primarily ascending auditory projections (DL, 2005; JF, 2001; Willard FH & DK, 1983) and two non-lemniscal divisions known as the dorsal (DC) and lateral (LC) cortices that receive massive descending auditory as well as multisensory input (Bajo & Moore, 2005; Coleman & Clerici, 1987; Loftus, Malmierca, Bishop, & Oliver, 2008; Saldaña, Feliciano, & Mugnaini, 1996; Christoph E Schreiner & Winer, 2005; Winer, Larue, Diehl, & Hefti, 1998). The LC and DC appear to differ in their strategy for integrating these inputs. The DC does not contain known structural heterogeneities, but has a tonotopic arrangement of neuronal responses on its surface (Barnstedt, Keating, Weissenberger, King, & Dahmen, 2015; Wong & Borst, 2019). In contrast, the LC contains repeated neurochemical motifs, here referred to as modules, that stain intensely for the inhibitory neurotransmitter GABA as well as other metabolic markers (Chernock, Larue, & Winer, 2004). Areas outside the modules, referred to as matrix, stain strongly for calretinin (Dillingham, Gay, Behrooz, & Gabriele, 2017). We and others have determined that nearly all of the long- and short-range connectivity of the LC is governed by the module/matrix organization (Dillingham et al., 2017; Lamb-Echegaray, Noftz, Stinson, & Gabriele, 2019; A. M. H. Lesicko, Sons, & Llano, 2020; A. M. Lesicko, Hristova, Maigler, & Llano, 2016). Unfortunately, how the LC integrates these inputs while maintaining distinct paths of information flow is not known. For example, LC neurons are known to respond to multisensory stimuli (Jain & Shore, 2006; Zhou & Shore, 2006), but information from different modalities enters the LC in segregated channels (A. M. Lesicko et al., 2016). Thus, integration across the module/matrix border must occur, but the mechanisms of this integration are unknown. Traditional methods of studying the LC, such as multichannel electrophysiology, pose significant challenges in unambiguously assigning individual recorded neurons to residence in

matrix or modules. Imaging approaches, such as two-photon (2P) microscopy, have proven to be enormously valuable in understanding the fine spatial structure of neural response properties in the auditory system (Bandyopadhyay, Shamma, & Kanold, 2010; Romero et al., 2020; Rothschild, Nelken, & Mizrahi, 2010). However, because of its superficial location on the dorsal surface of the mouse midbrain, the DC is the only part of the IC that has been characterized by 2P imaging (Barnstedt et al., 2015; Ito, Hirose, Murase, & Ikeda, 2014; Wong & Borst, 2019). Optically, it has been impossible to characterize the functions of the LC, which is laterally embedded deep in a brain sulcus. This inability to image the LC impedes our knowledge about how the LC performs the critical tasks of segregation and integration, whether neurons in the modules or surrounding matrix have different response properties or whether tonotopy or other spatial structure in response properties exists. Here, we describe a novel approach using a 45° microprism inserted into the sulcus that separates the LC from the cerebellum to investigate the fine-scale functional organization of the LC from its lateral surface through 2P imaging. The 2P images obtained from the microprism revealed the first ever images of the LC in vivo showing its characteristic GABAergic modules. Compared to the DC imaged from the surface, the acoustically evoked calcium signals obtained by the 2P imaging of the LC through the microprism revealed functional distinctions between the LC and DC. To accomplish this goal, we solved several technical challenges, including working in a highly vascular area and imaging a structure which is seated deep relative to the overlying skull. This novel method will provide neuroscientists a new experimental approach to optically examine and manipulate the auditory and non-auditory functions of the LC and/or its inputs or other brain regions hidden in sulci or other inconvenient locations.

Results:

The insertion of 45º microprism for imaging the LC from the side.

GAD67-GFP knock-in mice were crossed with Thy1-jRGECO1a mice to produce a GAD67-GFPxjRGECO1a hybrid mouse, which was used to visualize GABAergic modules, which is important to identify the LC, in the green channel (Tamamaki et al., 2003) and the calcium indicator, jRGECO1a, in the red channel (Dana et al., 2018). A standard craniotomy was performed (Goldey et al., 2014) with modifications to suit the specific characteristics of the IC in terms of its location, depth, and the high density of the surrounding vasculature (Xiong et al., 2017). The craniotomy was large enough (~ 3 x 4 mm) to not drill directly into the sagittal and lambdoid sutures which allowed minimal disruption of the superficial sinuses below the skull (Figure 1A) as indicated with the minimal bleeding near the bone flap (Figure 1B). During drilling, pressurized air and a cold stream of saline were used to remove the bone debris and dissipate heat. Because the IC sits deeper in the brain compared to the surrounding structures, the direct insertion of the 45º microprism was found to push the IC ventrally. Therefore, a fine diamond knife was used to separate the lateral surface of the IC from the cerebellum without damaging the transverse and sigmoid sinuses (Figures 1 C and D). This step was followed by a gentle retraction of the knife medially to generate a pocket to secure the microprism (Figure 1E). The successful insertion of the microprism was assessed by examining the reflection of the diamond knife from the microprism's top glass surface (Figures 1F and G). Holding the microprism down and retracting the knife upward simultaneously resulted in securing the microprism in its pocket (Figure 1H). Locking the microprism down in its pocket for 10 minutes by the diamond knife (Figure 1J) is critical to ensure that the microprism is stabilized and to prevent bleeding. Filling the gap between the skull surface and the microprism with saline was found to generate motion artifact due to the heart pulsation, so 1% agarose was used to fill the gap to reduce the motion artifact and add more stability to the microprism (Figure 1K). To

compare response properties between the LC and DC, direct imaging (i.e., without a microprism) of the dorsal surface of the IC, where the DC is located, was also conducted (Figures 1L and M).

Figure 1: A brief Illustration of the surgical procedures.

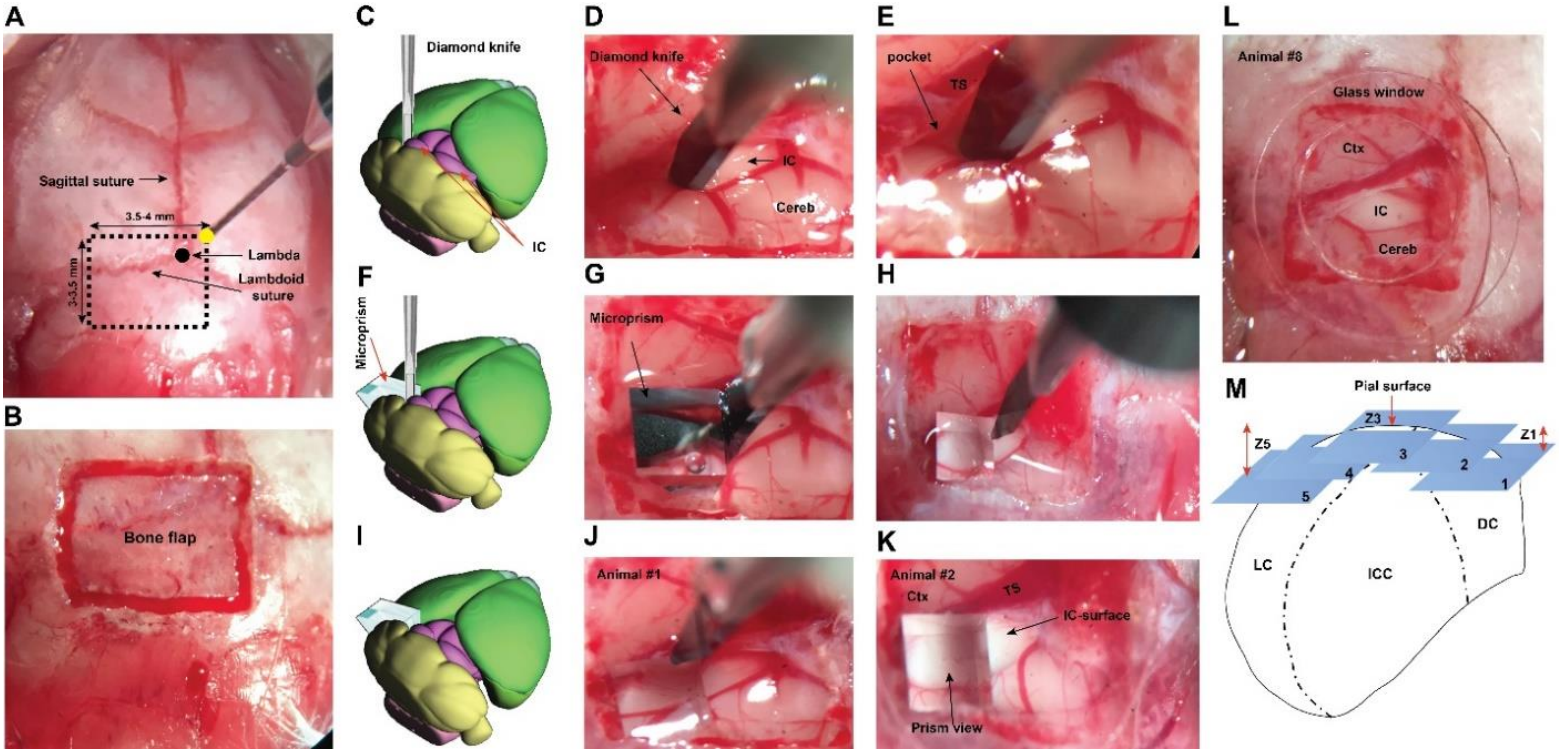

(A) A surface view of the mouse's skull showing the landmarks of the craniotomy over the IC. (B) An image of the bone flap after finishing the drilling. (C-E) A cartoon and two images of the brain surface showing the insertion and the pocket made by the diamond knife at the lateral surface of the left IC. (F-H) A cartoon and two images of the brain surface showing the insertion of the microprism into its pocket to directly face the LC after displacing the blade of the diamond knife. (I-K) A cartoon and two images of the brain surface showing the final setup of the microprism for two different animals. (L) An image of the brain surface showing the placement of a glass window for the surface imaging the DC. (M) A cartoon of the coronal section of the IC demonstrating the different field of views taken along the mediolateral axis parallel to the curvature of the IC surface at different depths (z1-z6) from the pial surface. Cereb: The cerebellum, Ctx: The cerebral cortex, DC: The dorsal cortex of the IC, IC: The inferior colliculus, ICC: The central nucleus of the IC, LC: The lateral cortex of the IC, TS: The transverse sinus.

The 2P characterization of GABAergic neuronal distribution on the LC and DC surfaces with a histological validation.

Following the surgery, the anesthetized animals were taken immediately for imaging. Examination of the distribution of GABAergic modules in the LC was critical to validate the target imaging area for functional calcium imaging. Therefore, the 920 nm laser beam was initially used to scan for GFP, which is expressed in the GABAergic cells of GAD67-GFP knock-in mouse. The insertion of the microprism was initially viewed by low magnification epifluorescence imaging of the GFP signals from the whole surface of the IC along with the inserted microprism (Figure 2A). This step validated the location of the microprism relative to the IC under the microscope, and to ensure there was no bleeding or blood clots that could block the field of view. The 2P images of the GFP signals from the LC imaged via the microprism (Figures 2C, D, and G) revealed the LC characteristic GABAergic modules, which were consistent with previous 3D reconstructions of modules from the coronal sections (Chernock et al., 2004; A. M. Lesicko et al., 2016). To further validate microprism location and the ability to image the LC from the lateral surface, a laser lesion (see Methods) was created via the microprism (Figure 3A), which was validated histologically (Figure 3B). For comparison, the whole dorsal surface of the IC was scanned from medial to lateral borders (Figure 2B, the dotted white lines). The mediodorsal part of the IC surface showed a non-clustered distribution of the GABAergic cells (Fig 2F and I-blue boxes), while the lateral horizon of the surface of the IC showed clusters of GABAergic cells and terminals into modules, the prominent feature of the LC (Figure 2E and H, red boxes). To further validate the presence of GABAergic modules in the lateral portion of the dorsal surface of the IC, a laser lesion was created in a GABAergic module located at the lateral dorsal surface (Figure 3C and D), which was confirmed histologically (Figure 3E), demonstrating that it is possible to image a portion of the LC from its dorsal surface.

Figure 2: The distribution of GABAergic cells om the LC imaged via microprism, and DC imaged from the surface.

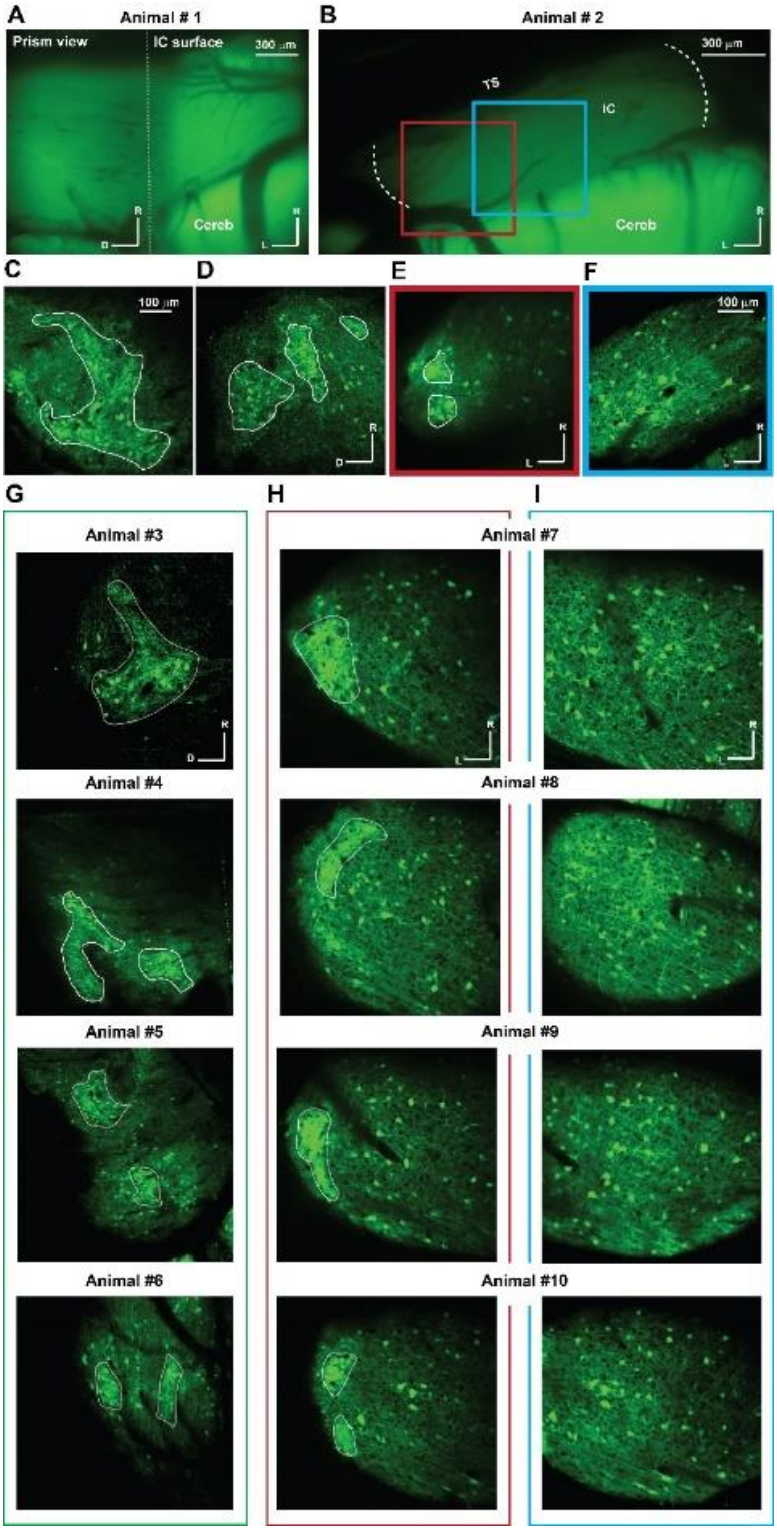

All images were taken for the GFP signals exclusively expressed in GABAergic cells. (A-B) Low magnification images for the GFP signals obtained from the IC surface with or without the microprism, respectively. The dotted white line in b represented the medial and lateral horizons of the IC. (C-D and G) The 2P images of the GABAergic cells on the LC imaged via microprism showing the GABAergic modules across multiple animals. (E and H) The 2P images of the GABAergic cells on the lateral top surface of the IC imaged from above showing the GABAergic modules across multiple animals (The red box in B). (F and I) The 2P images of the GABAergic cells on the medial dorsal surface of the IC imaged from above showing a homogenous distribution of GABAergic cells of different size with no signs of the GABAergic modules across multiple animals (The blue box in B). All solid irregular white lines were made at the border of the GABAergic modules; D: Dorsal, L: Lateral, R: Rostral.

Figure 3: The validation of imaging setup.

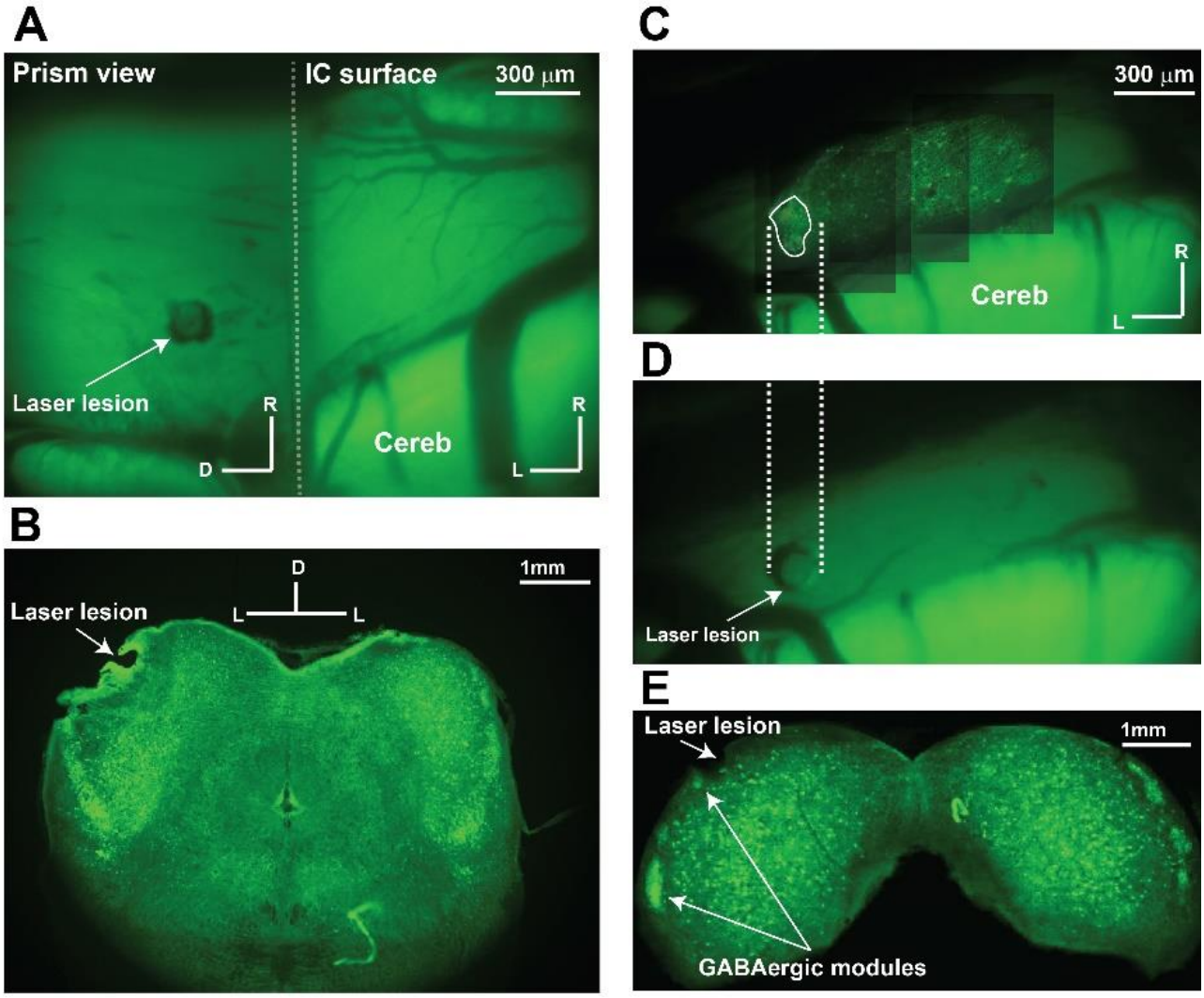

All images were taken for the GFP signals exclusively expressed in GABAergic cells. (A) A low magnification image of the IC surface with the microprism showing a laser lesion spot made through the microprism to validate the position of the microprism relative to the IC. (B) A histological coronal section at the level of the IC showing that the laser lesion made by the microprism was located at the sagittal surface of the LC. (C-D) Low magnification images of the IC surface without the microprism showing a laser lesion spot made on the dorsal surface of the LC near one of the GABAergic modules. The dotted white lines represent the alignment of the laser lesion to the location of the GABAergic modules at the lateral top surface. (E) A

histological coronal section at the level of the IC showing that the laser lesion made on the IC surface targeted one of the GABAergic modules at the on the dorsal portion of the LC. The solid irregular white line was made at the border of the GABAergic modules.

Dorsal and lateral cortices differently respond to sound.

As expected, the hybrid mouse showed a non-clustered cellular expression of jRGECO1a, on the surface of the DC (Figure 4A) or on the surface of the LC imaged via microprism (Figure 4B). The IC of anesthetized animals in each experimental setup was then imaged to measure calcium signals over the course of pseudorandom presentations of either 500 ms pure tone of different combinations of frequencies (5-40 kHz, half octave intervals) and sound levels (40-80 dB SPL, 10 dB intervals) or amplitude-modulated broadband noise (AM-noise) of different combinations of modulation frequencies (2-256 Hz, one octave intervals) and sound levels (40-80 dB SPL, 10 dB intervals). As shown by two representative cells from the DC or LC, these acoustic stimulation paradigms successfully elicited transient cellular calcium signals that varied depending on stimulus type (Figures 4C and D).

Figure 4: The 2P expression of jRGECO1a along with evoked signals at the LC vs DC.

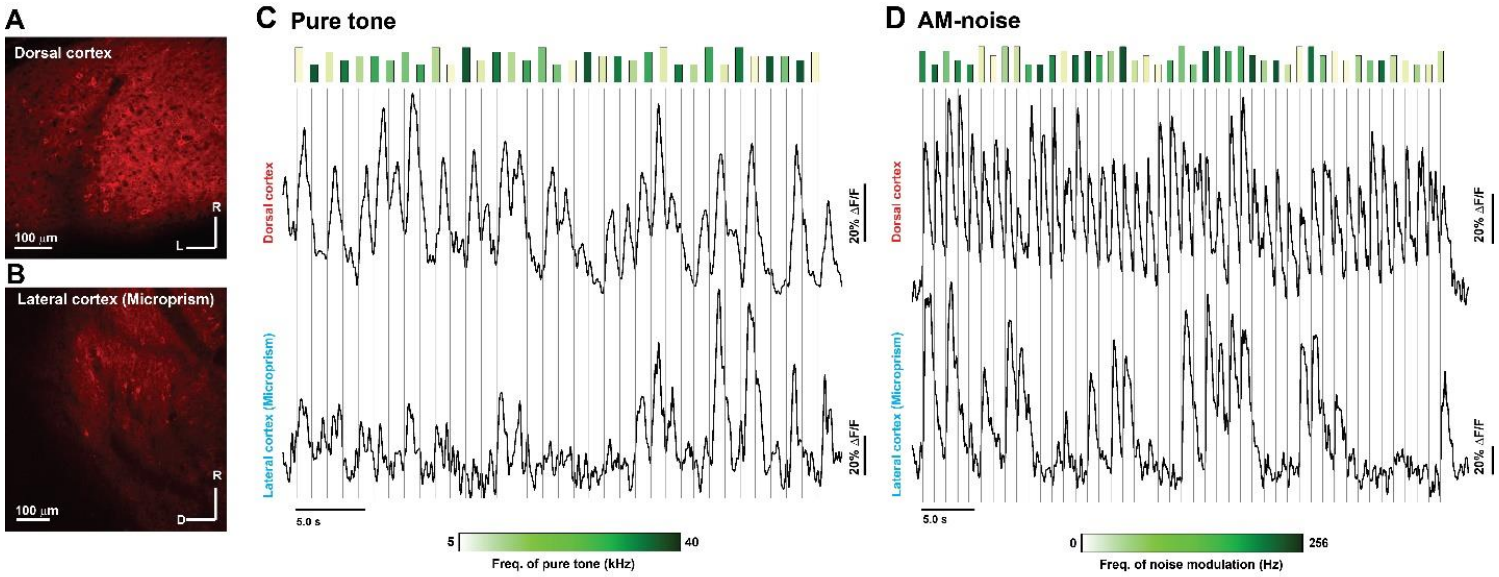

(A-B) The 2P images of the jRGECO1a expression on the DC imaged from the dorsal surface and the LC imaged from the lateral surface via a microprism, respectively. (C-D) The time traces of the evoked calcium signals by different stimuli of either pure tone or AM-noise, respectively, which were obtained from two different cells on the DC imaged from the surface (top traces) or LC imaged via microprism (bottom traces); The length of the gradient green bars (top) indicates the intensity of the stimulus, while the color intensity indicates the frequency depending on the color scale (bottom).

As indicated by the GFP signals, the hybrid mice showed clusters of GABAergic modules on the lateral surface of the LC imaged via a microprism (Figure 5A, irregular white lines) or from the lateral-most dorsal surface of the IC (Figure 5D, irregular white lines). Based on the best pure tone frequency of each responsive cell (Barnstedt et al., 2015), the DC showed a tonotopic organization of cells along the rostromedial to caudolateral axis tuned to lower or higher frequencies, respectively (Figure 5E). This tonotopic organization is similar to those previously described (Barnstedt et al., 2015; Wong & Borst, 2019). In contrast, the LC cells imaged via the

microprism did not show a tonotopic organization (Figure 5B). To quantify tuning differences between DC and LC, the distribution of the cells based on their best frequency was compared. Consistent with the visual assessment of figures 5B and E, the cumulative distribution function showed that while 60% of the DC was tuned to 5kHz, the lowest tested frequency, most of the LC cells imaged via microprism were tuned to higher frequencies (Figure 6A, Two-sample Kolmogorov-Smirnov Test: d = 0.42, *p = 1.02×10^{-31} for DC vs LC), which suggests that the lateral view of the LC imaged via microprism is an extension of the LC measured directly from the lateral-most portion of the dorsal surface of the IC, which was also tuned to higher frequencies. These data are also consistent with previous electrophysiological recordings done on mice (Romand & Ehret, 1990; Stiebler & Ehret, 1985) showing that while the dorsal surface of the IC is mostly tuned to low frequencies, the tuning was shifted to higher frequencies by moving ventrally.

To measure responses to complex sounds, LC and DC neuronal responses to AM-noise were measured, and revealed that a significant fraction of cells that did not respond to tones did respond to AM-noise. This is apparent visually in figures 5C and f versus figures 5B and E, and quantitatively by computing the fraction of the responsive cells to both stimuli from each region (Figure 6B, Mean ± SEM: 77.8%±3.6 vs 96.6%±0.85 (DC) & 16.2%±4.3 vs 37.1%±5.5 (LC) for pure tone vs AM-noise & 87.2±3.9 vs 26.6%±4.5 for DC vs LC, two-way ANOVA, f (1, 1, 16) = 171.8, 18.4, 0.04 & p = 5.7×10^{-10}, 5.5×10^{-4}, and 0.83, for region, stimulus type, and interaction, respectively, Fisher post hoc test: $^{\#}p = 4.2 \times 10^{-4}$ for pure tone & AM-noise & $^{*}p = 5.6 \times 10^{-10}$ for LC vs DC). Additionally, based on the cell's best AM frequency, more cells in the LC and DC were responsive to AM-noise compared to the non-modulated noise (Figures 5C and F, mean ± SEM: 37.0%±1.6 vs 63.0%±1.6 (DC) & 17.5%±2.4 vs 82.4%±2.4 (LC) for unmodulated vs AM-noise, two-way ANOVA, f (1, 1, 16) = 0, 381.3, 69.8 & p = 1.0,1.3×10^{-12}, and 3.1×10^{-7}, for region, stimulus type, and interaction, respectively, Fisher post hoc test: p = 2.8×10^{-13} for unmodulated

& AM-noise). Collectively, this increase in the responsiveness of the cells in both regions with increasing sound complexity is consistent with the idea of the LC and DC as being non-lemniscal integrative regions (C. Chen, Cheng, Ito, & Song, 2018; Faye-Lund & Osen, 1985; Loftus et al., 2008). However, it is interesting to note that a strip exists in the medial portion of the DC, extending from its caudal to its rostral border, where most of the cells were only responsive to non-modulated noise (Figure 5F). This novel finding suggests that the response of the DC surface could be mapped based on the complexity of sound stimulus and there were some discrete locations on the IC surface that could be sensitive to specific temporal features of sound.

Regardless of the sound type, a lower fraction of neurons was responsive to the acoustic stimulation in the LC imaged via microprism compared to DC (Figure 6B). To evaluate if any optical artifacts due to imaging through a prism could be responsible for this difference, the number of responsive cells imaged from the lateral-most dorsal surface of the IC, which we consider part of the LC because of the presence of GABAergic modules, and because its best frequency distribution matches that of the LC imaged from the lateral surface, was quantified and compared with that obtained from the LC imaged via microprism. We compared these two fractions of responsive cells with that obtained from the bulk of the DC medial to the modules. We observed that neurons in the DC were more responsive than neurons in the LC measured either via microprism, or directly on the dorsal surface (Figure 6C, Mean ± SEM: 78.5±11.0, 49.2±8.7, 26.5%±6.9 for DC, LC imaged on dorsal surface, and LC imaged via microprism, one-way ANOVA, $f(2, 9) = 8.3$, $p = 0.009$, Fisher post hoc text: *$p = 0.0028$ and 0.0477 for DC vs LC [via microprism] or LC [on dorsal surface], respectively; $p = 0.11$ for LC via microprism vs. LC on dorsal surface). These data suggest that the diminished proportion of responsive cells observed in the LC when imaged through the microprism is not an artifact of imaging them indirectly, and likely reflects a difference between LC and DC.

Further examination of the LC imaged with a microprism revealed that the modules contained a higher fraction of sound-responsive cells than the matrix (Figure 6D-right, Mean ± SEM: 36.9%±7.3 vs 16%±5.3 (pure tone) & 66.9%±7.4 vs 46.9%±8 (AM-noise) for modules vs matrix, two-way ANOVA, $f(1, 1, 12) = 8.3, 18.3, 0.003$ & $p = 0.01, 0.001$, and 0.95, for region, stimulus type, and interaction, respectively, Fisher post hoc test: $^{*}p = 0.013$ for modules vs matrix). This finding was unexpected given that modules receive less direct auditory inputs compared to matrix (A. M. Lesicko et al., 2016). That said, local module-matrix network connectivity has been described and many LC neurons have dendritic branches that extend beyond module/matrix borders (A. M. H. Lesicko et al., 2020). These data suggest that greater-than-expected crosstalk occurs across the module/matrix border – a result that could only be revealed with the approaches described herein. We did not observe differences in best frequency distribution (Two-sample Kolmogorov-Smirnov Test: $d = 0.152$ & $p = 0.297$) or the best modulation frequency distribution (Two-sample Kolmogorov-Smirnov Test: $d = 0.107$ & $p = 0.33$) across the module/matrix border. However, a higher fraction of cells in matrix was exclusively responsive to AM-noise compared to pure tones (Figure 6D-left, Mann-Whitney Test: $z = -2.3$, $^{*}p = 0.021$), which suggests that neurons in the matrix may be more sensitive to complex sounds compared to those in the modules.

Figure 5: The response of the LC vs DC to different acoustic stimulations.

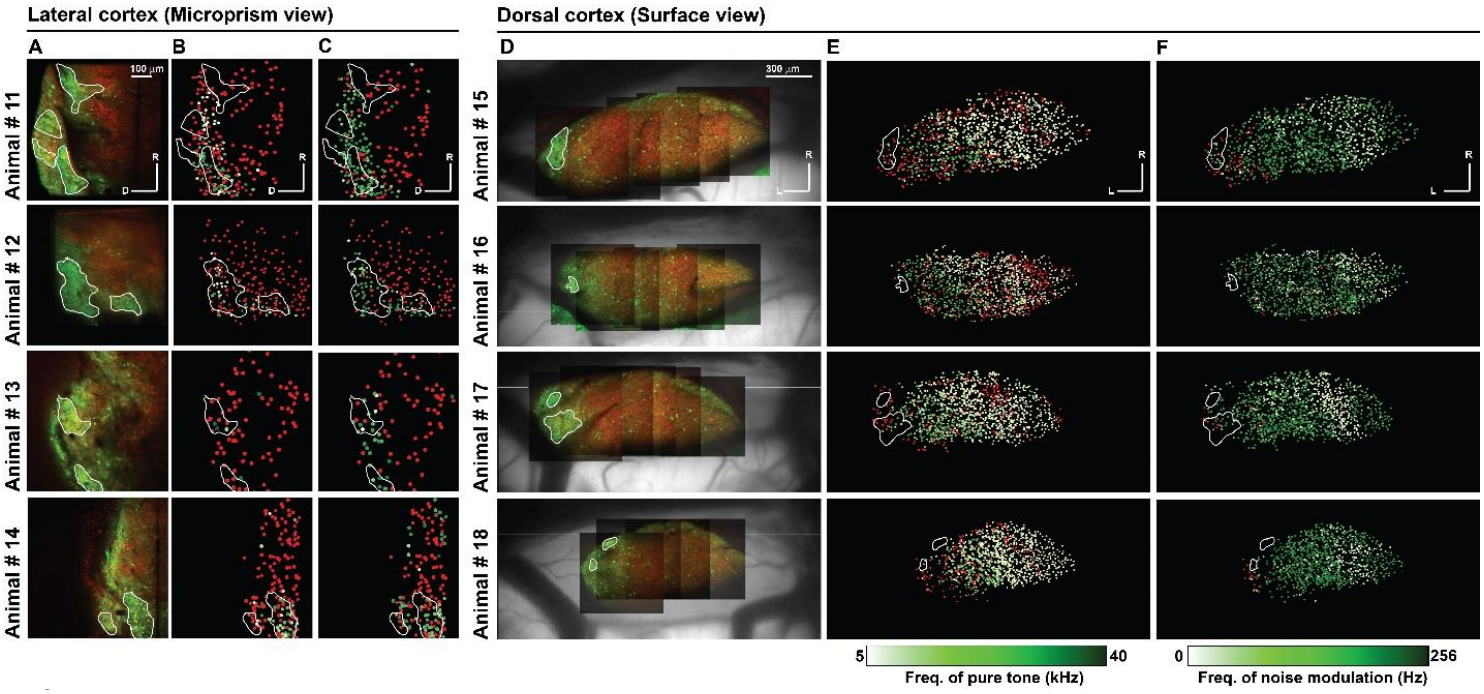

(A and D) The superimposed 2P images of both GFP and jRGECO1a signals from the LC imaged via a microprism and DC imaged from the surface, respectively, across different animals. (B and E) Aligned with the 2P images in a and b, the pseudocolor images show the activity of the cells on the LC and the DC, respectively, across different animals in response to the pure tone based on their best frequency as graded green circles for the responsive cells and solid red circles for the non-responsive cells. (C and F) Aligned with the 2P images in a and b, the pseudocolor images show the activity of the cells on the LC and the DC, respectively, across different animals in response to AM-noise based on their best modulation frequency as graded green circles for the responsive cells and solid red circles for the non-responsive cells. All solid irregular white lines were made at the border of the GABAergic modules.

Figure 6: The DC and LC could be functionally distinct.

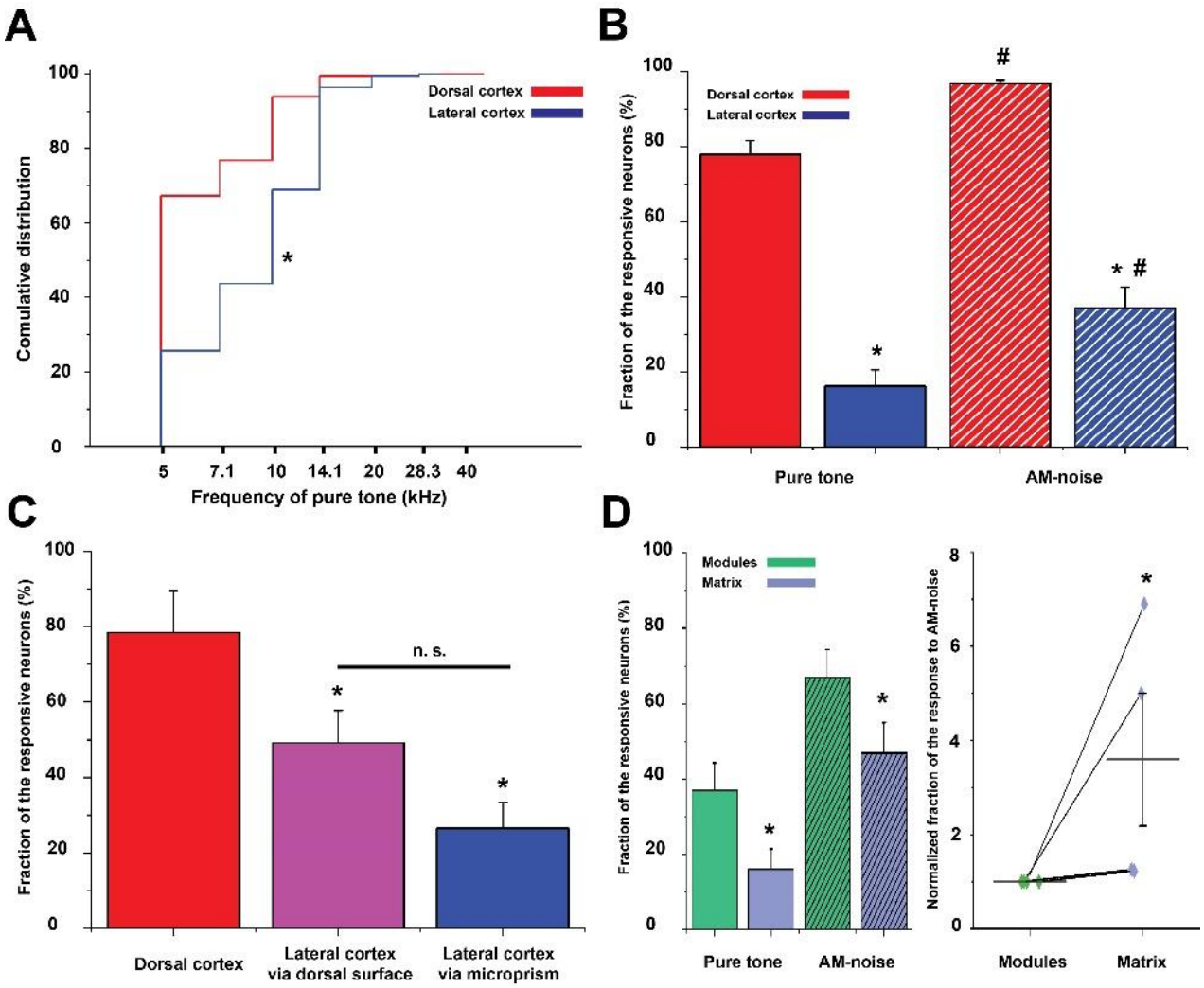

(A) The cumulative distribution function of the best tone frequencies of all cells collected either from the LC imaged via microprism (blue) or the DC imaged at the surface (red). (B) A bar graph showing the fraction of the responsive cells on the LC imaged via microprism (blue bars) vs the DC (red bars) against either the pure tone (solid color bars) or AM-noise (striped color bars) stimuli. (C) A bar graph showing the fraction of the responsive cells on the LC imaged via microprism (blue bar), the LC via the dorsal surface (purple bar), and the DC (red bar) imaged from the dorsal surface in response to pure tone stimuli. (D) Left: A bar graph showing the fraction of the responsive cells on the LC imaged via microprism at matrix (gray bar) or modules

(green bar) against either the pure tone (solid color bars) or AM-noise (striped color bars) stimuli. Right: A scatter graph showing the normalized fraction of the cells responsive to the AM-noise in matrix compared to modules.

Discussion:

Optical access to the brain is important for understanding how the brain works at a mechanistic level. Therefore, different cranial window and microscopic approaches have been developed to overcome the challenges related to the light penetration to the deep brain tissues (Cramer et al., 2021; Yang & Yuste, 2017). Multiphoton microscopy allows the simultaneous monitoring of hundreds of neurons on the surface of brain structures (Akerboom et al., 2013; Centonze & White, 1998; J. L. Chen, Andermann, Keck, Xu, & Ziv, 2013; Horton et al., 2013; Ouzounov et al., 2017). However, many brain regions are not yet optically accessible because of their orientation (cortical column), deeper location (subcortical structures) or surface topography (folded surfaces or sulci). Therefore, optical extenders such as gradient-index lenses, microprisms, or microperiscopes have been developed to facilitate imaging of these surfaces (Cramer et al., 2021; Redman et al., 2022). Given **its** ability to reflect the light at its hypotenuse, microprism based two-photon microscopy has been successfully used to image the six cortical layers in the somatosensory and visual cortices of mice (Andermann et al., 2013). and to image other inaccessible cortical surfaces like those folded in the brain sulci such as the medial prefrontal cortex (Low, Gu, & Tank, 2014) or entorhinal cortex (Beckmann et al., 2019; Heys, Rangarajan, & Dombeck, 2014; Low et al., 2014). In those studies, the glass window glued to the microprism was used, which requires significant skill and potentially removal of brain regions to allow prism access (Heys et al., 2014). Another approach is to use a micro metal or diamond-made knife to create a pocket with minimal tissue damage (Andermann et al., 2013; Marks & Goard, 2021). Accordingly, we combined and modified some of these procedures to improve the microprism implantation to image the surface of the LC, which is deeply embedded into the

brain tissue in a highly vascular area, with minimum damage to the IC or the surrounding vasculature. In mice, the IC sits lower than the surrounding structures by ~ 1 mm, which made it impossible to insert a 1x1 mm microprism, so a larger microprism (1.5x1.5 mm) had to be used. Therefore, the direct implantation of this microprism into the brain tissue (Beckmann et al., 2019; Heys et al., 2014; Low et al., 2014) resulted in bleeding and excessive depression of the tissue. Due to the IC location, it was also not possible to glue the microprism to a circular glass window as one unit. Therefore, some modifications have been made. First, a micro diamond knife was carefully used to separate the connective tissue surrounding the IC to make an initial separation. The diamond knife was then gently retracted medially leaving a small pocket for the microprism to fit in with a minimal chance of tissue damage. After the microprism's implantation, the upward retraction of the knife left the microprism to face the LC surface directly from the lateral surface. Second, the gap was filled with 1% agarose gel, which is known for its high optical penetration, minimum autofluorescence, and good reflectance contrast (Bal, Andresen, Baggett, & Utzinger, 2013). These modifications gave the microprism the freedom to access deeper tissues allowed a greater flexibility in the setup design, and is suitable for long-term imaging (Holtmaat et al., 2009).

Previous work using microprisms have been done chronically for up to 60 days (Heys et al., 2014; Low et al., 2014; Wenzel, Hamm, Peterka, & Yuste, 2017), with minimal tissue inflammation (Andermann et al., 2013). The current study was done on anesthetized animals to initially examine and validate the new modifications. Given that the IC responses to sound across different species may be sensitive to the arousal state or to different anesthetics (Astl, Popelár, Kvasnák, & Syka, 1996; C. Chen & Song, 2019; Ter-Mikaelian, Sanes, & Semple, 2007), a future direction is to replicate this work in awake behaving animals.

Although imaging through a microprism and 1-mm cover glass appear to have minimal impact on image quality compared to direct two-photon imaging (Chia & Levene, 2009), it was

important to compare LC imaging via microprism with the direct 2P imaging of the dorsal-most portion of the LC from the surface to validate the new imaging method. We found no significant differences between LC response properties when imaging via a microprism or imaging directly. Interestingly, however, we did observe significant differences between the LC and the DC. Despite the low frequency bias of the DC cells (Figure 6A), the DC has a tonotopic organization of cells tuned to lower and higher frequencies along the mediolateral axis, which was consistent with previous results (Barnstedt et al., 2015; Wong & Borst, 2019). This tonotopic distinction between LC and DC was consistent with electrophysiological studies done on mice (Romand & Ehret, 1990; Stiebler & Ehret, 1985). Although both the LC and DC preferentially responded to AM-noise compared to pure tones, only the DC was found to map its response to different modulation frequencies. These data suggest that a form of periodotopy may be present on the surface of the IC. These data are intriguing given previous work suggesting the existence of periodotopy in the body of the IC (Baumann et al., 2011; C. E. Schreiner & Langner, 1988). Future work should examine how these various periodotopic maps are linked. In summary, a novel imaging method has been developed to image the LC surface via microprism. This modification in the microprism implantation can be applied to other brain surfaces such as the sulci of both cortex and cerebellum, caudal parts of the hippocampus, or any other similar brain regions.

Materials and methods:

Animal subjects:

Male mice of 6-12 weeks of age were used. GAD67-GFP knock-in mice (developed and shared with permission from Dr. Yuchio Yanagawa at Gunma University and obtained from Dr. Douglas Oliver at University of Connecticut), where GFP is exclusively expressed in the GABAergic cells (Tamamaki et al., 2003), was used to visualize the GABAergic cells and LC modules. To simultaneously monitor the calcium imaging and visualize the GFP signals, Tg(Thy1-

jRGECO1a)GP8.20Dkim/J mice (Jackson Laboratory, Stock# 030525) were crossed with GAD67-GFP knock-in mice to generate GAD67-GFPxThy1-jRGECO1a hybrid mice. The mice were housed and bred at the animal research facility of The Beckman Institute for Advanced Science and Technology. The animal care facilities approved by the Association for Assessment and Accreditation of Laboratory Animal Care (AAALAC). To phenotype the GFP positive animals, an epifluorescence microscope was used for the transcranial examination of the pups at postnatal day 4 using 470 nm filter at low power magnification (2x, Olympus objective). The positive pups exhibited a green fluorescence in the cerebellum, the cerebral cortex and the olfactory bulb were only kept with their parents until weaning. The genotyping for jRGECO1a was done using a probe composed of a forward primer: GCCGCCGAGGTCAAGA & a reverse primer: TCCAACTTGATGTCGACGATGTAG) by Transnetyx™ (Transnetyx, USA). Samples of the mice tail snips around one month of age were used for genotyping. All applicable guidelines for the care and use of animals were followed. All surgical procedures were approved by the Institutional Animal Care and Use Committee (IACUC).

Surgery

The general procedures of craniotomy were previously described (Goldey et al., 2014), with modifications to place craniotomy over the IC. Before surgery, mice were anesthetized with a mixture of ketamine, xylazine, and acepromazine (100 mg/kg, 3 mg/kg, and 3mg/kg, respectively) delivered intraperitoneally. The anesthesia was maintained during the surgery and imaging using only ketamine (100 mg/kg). To prevent neural edema during or after the craniotomy, an intramuscular injection of dexamethasone sodium (4.8 mg/kg) was given just before the surgery using an insulin syringe. After placing the animal in the stereotaxic apparatus (David Kopf Instruments, USA), both eyes were protected by applying Optixcare lubricant eye gel (Aventix Animal Health, Canada). The hair of the scalp was then removed by massaging the scalp with a depilatory cream (Nair) using a cotton-tipped applicator and leaving the cream on

the scalp for 4-5 minutes. The cream was then removed by a thin plastic sheet (flexible ruler) to leave a hair-free area on the scalp**.** The remaining tiny hair was then removed by alcohol swab and the area was then sterilized by applying 10% Povidone Iodine (Dynarex, USA) using a sterile cotton-tipped applicator. The medial incision was made with a scalpel blade #10, and 0.2 ml of 0.5% lidocaine was injected intradermally in the scalp. The skin extending from the medial line to the temporalis muscle was completely removed using a pair of microscissors to produce a wide skinless area above the skull. A pair of no. 5/45 forceps were used to remove any remaining periosteum. The remaining dried or firmly attached pieces of periosteum were removed with a scalpel blade #10. The skull was cleaned with a sterile saline and dried with a gentle pressurized air. Using the stereotaxic apparatus, a wide area of ~3 x 4 mm above the left IC was made. A micro drill bit (Size #80, Grainger, USA) was used to drill through the skull starting from the rostrolateral (Figure 1A, yellow circle) region to lambda (Figure 1A, black circle) following the border in a clockwise direction (Figure 1A, dotted black rectangle). To prevent overheating of the superficial brain tissues and to mitigate the occasional spurts of skull bleeding during the drilling, an ice-cold sterile saline was used to intermittently irrigate the surface. A stream of a pressurized air was also applied also during the drilling procedures to prevent overheating and to remove the debris produced by the drilling. Caution was taken not to pierce the dura when performing the craniotomy while crossing the sagittal or the lambdoid sutures to avoid damaging the underling sinuses. After drilling, the skull was irrigated in a sterile saline and the bone flap (the undrilled bone over the craniotomy area) was gently examined for the complete separation from the rest of the skull (Figure 1B). Using a pair of no. 5/45 forceps, the bone flap was gently removed. To control the bleeding if it occurred, a piece of sterile hemostatic gel (Adsorbable Gelatin Sponge USP, Haemosponge, GBI, India) which was pre-soaked in an ice-cold saline, was applied to the bleeding spot. Once the bleeding ceased, the brain was kept covered in a sterile saline. In some surgeries, the dura was peeled off from the surface of the IC while removing the bone flap. In the surgeries where dura remained intact, a

Bonn microprobe (F.S.T, Germany, Item # 10032-13) was used to pierce the dura in an area that is not above the IC and devoid of cortical vasculature (e.g., a part of exposed cerebellum). After piercing, the dura was carefully and gently lifted, and a pair of no. 5/45 forceps were used to grab the dura to gently tear it to the extent of the transverse sinus to avoid bleeding of that major vein.

Using the stereotaxic apparatus, a 30° diamond knife (F.S.T, Germany, Item # 10100-30) was placed in its vertical position. From the medial line, the knife was placed at the lateral horizon of the IC. The knife was then inserted 1.5 mm ventrally. Extreme caution was taken to avoid hitting any major blood vessels to avoid bleeding. From its position, the knife was 0.3-0.5 mm retracted medially to create an initial pocket for the insertion of the microprism (Figures 1C-E). The microprism (1.5 mm-silver coated, Tower Optical Corporation) was then inserted, so one of its sides was parallel to the lateral surface of the diamond blade, the other side was facing up, and its hypotenuse was facing ventrally (Figures 1F and G). The wooden piece of a cotton swab was carefully driven down to push the microprism until its top surface was at the same level of the IC dorsal surface. Keeping the microprism in its place with the wooden end of a swab, the diamond knife was carefully retracted upward leaving the microprism behind (Figure 1H). If the retraction of the diamond knife pulled the prism up, the wooden piece would be used to push it down simultaneously with the knife movement. To control the bleeding, a piece of sterile hemostatic gel was used as before. The tip of the diamond knife was used to secure the microprism in its position for at least 10 minutes (Figures 1I and J). During that time, the solution of the 1% agarose was made to be ready for use. A pair of forceps was then used to gently place a sterile 5 mm cover glass #1 (Thomas Scientific, USA) over the skull covering the opened area above the IC. The cover glass was secured by a wooden trimmed piece of sterile cotton swab by gently pressing the cover glass from the top. Since the surface of the IC was located below the surfaces of both cerebellum and cerebral cortex, the cover glass usually traps about 0.7-1.0 mm

thick sheet of sterile saline. The movement of the liquid medium caused by heart pulsation was found to be a source of motion artifact during imaging, so the gap between the surface of the IC and the cover glass was filled with 1% agarose gel that was made in saline at a temperature range of 33-35°C (Figure 1K). The extra agarose gel pieces were cut off and removed by the scalpel blade and the wet skull was then dried out using a pressurized air. A titanium headpost as described before (Goldey et al., 2014) was glued carefully on the top of the skull to be at the same level of the cover glass. Following the manufacturer instructions, the C&B Metabond (Parkell, Japan) was used to secure the headpost in its place. Excluding the steps of the microprism insertion, the same procedures were followed for the DC imaging from the surface (Figure 1L).

Acoustic stimulation:

Using a custom-made MATLAB (The MathWorks, Natick, MA, USA) code, either 500 ms pure tone or AM-noise were generated. Thirty-five (5x7) pure tones with a series of sound pressure levels (80, 70, 60, 50 ,40 dB SPL) and a series of carrier frequencies (5000-40000 Hz with a half octave gap) were presented with a cosine window. Forty-five (5x9) 100% amplitude-modulated white noise bursts with a series of sound pressure levels (80, 70, 60, 50 ,40 dB SPL) and modulation frequencies (0, 2, 4, 8, 16, 32, 64, 128, 256 Hz) were generated. The stimuli of either pure tone or AM-noise combinations were played in random sequence to the mice with a 600 ms interstimulus interval by a TDT RP2.1 processor (Tucker-Davis Technologies, US) and delivered by a TDT ES1 speaker (Tucker-Davis Technologies, US).

Two-Photon imaging:

Immediately after surgery, the anesthetized animal was taken and secured under the microscope objective by clamping the arms of the head post to two perpendicular metal post mounted on the microscope stage. A custom-built 2P microscope was used. The optical and the controlling components were supplied from Bruker, Olympus, and Thorlabs. The imaging of the

DC was made using a 20X water-immersion objective (LUMPlanFI/IR, 20X, NA: 0.95, WD: 2 mm; Olympus Corporation, Tokyo, Japan), while the lateral surface of the IC was imaged by the long working distance 16x water-immersion objective (N16XLWD-PF - CFI LWD Plan Fluorite Objective, 16X, NA: 0.8, WD: 3.0 mm; Nikon, Tokyo, Japan) to be able to reach the focal point of the microprism at its hypotenuse. For imaging both the GFP or jRGECO1a signals, the excitation light was generated by InSight X3 laser (Spectra Physics Lasers, Mountain View, CA, USA) tuned to a wavelength of 920 or 1040 nm, respectively. A layer of a 1:1 mixture of Multipurpose wavelengths ultrasound gel (National therapy, Canada) with double deionized water was used to immerse the objective. This gel was able to trap the water and reduce its evaporation during imaging. The emitted signals were detected by a photomultiplier tube (Hamamatsu H7422PA-4, Japan) following a t565lp dichroic and a Chroma barrier et525/70m filter for GFP and et595/50m filter for jRGECO1a signals. Images (512x512 pixels) were collected at a frame rate of 29.9 Hz at the resonant galvo mode. Data were collected from the dorsal surface of the IC by scanning the surface of the IC based on the GFP and jRGECO1a signals through the medial and lateral horizons of the IC. Generally, the scanning was started by moving the 20x objective to the most ventromedial position, where there is no ability to see any cells (Figure 2B, medial horizon). Then, the objective was started to slowly move dorsolaterally to get cells in focus (Figure 1M), where the average depth of the first field of view was 169 μm. The lateral movement of the objective was intended to be aligned and parallel to the curvature of the DC surface indicated by getting the superficial cells in focus to avoid any possibility for imaging the upper layers of the central nucleus of the IC, so the average depth of the most superficial point of the imaging was 92 μm. The scanning was ended by moving the objective to the most ventrolateral position of the IC, where there is no ability to see GFP laterally (Figure 2B, lateral horizon), where the last field of view was collected at an average depth of 225 μm. Generally, each field of view was selected based on the expression of GFP signals as an

indicator for the cells in focus and being acoustically active by using a search stimulus that was 500 ms broad band noise with zero modulation at 80 dB SPL. The z-axis of the objective was determined relative to the pia surface. The relative position of each region was tracked through the micromanipulator (MP-285, Sutter Instruments) that controlled the microscope objective. The positions of imaged areas were further aligned across animals to a common coordinate using the midline, lateral extremes, and the vasculature landmarks taken via imaging of the GFP signals of the cranial window with low magnification (4x Olympus objective, 4x4 binning, 50 ms frame time) using a Lumen 200 bulb (Prior Scientific Inc, USA) and CoolSNAP MYO camera (Photometrics, USA, excitation: 488 nm and emission: 515–550 nm). Imaging of the lateral surface of the IC via the microprism was done similarly. However, a 16x objective with long working distance was used to enable reaching the focal point at the microprism hypotenuse. For a good visualization of the cell bodies using the 16x objective, a digital zoom in (19%) was conducted using the controlling software (PrairieView 5.5). In both cases, the frame timing of the scanner and the sound stimuli were both digitized and time-locked using a Digidata 1440A (Molecular Devices, Sunnyvale, CA, USA) with Clampex v. 10.3 (Molecular Devices, Sunnyvale, CA, USA).

Laser lesion:

The laser lesion was done using a 720 or 820 nm laser beam at 74-80 mW power at the level of the objective for 100 to 250 seconds depending on the size of the lesioned area, the speed of laser scanning (frame rate), and the depth of the lesion (z-axis length). In brief, the area of interest and the dimension of the laser lesion were initially determined using 920 nm as indicated by the GFP signals through scanning one of the GABAergic modules. The depth of the GABAergic modules was then determined by counting the optical slices starting from its superficial surface. The tunable laser was then switched from 920 nm to the shorter wavelength (720 or 820 nm) to scan the same area and depth with a rate (1-2 frames/ second).

Data processing:

Data collection: The data were collected as separate movies (512x512 pixels) for each pure tone or AM-noise runs in a resonant galvo mode. Depending on the amplitude and frequency combinations for each type of the acoustic stimulus, 40- or 52-seconds periods were assigned as a movie's length for pure tone (35 stimulus combinations), or AM-noise (45 stimulus combinations), respectively. Using Image J software, the z-projection was used to compute one single image representing either the sum, the standard deviation, or the median of all the image sequences in the movie. Based on these single images, the region of interest (ROI) was manually drawn around each detectable cell body. Figures 4A and B represent the sum of the images sequences of the movie collected from the dorsal surface, or the lateral surface of the IC via microprism, respectively. For the subsequent processing steps, Python open-source libraries were used (listed below).

Motion Correction and Filtering: The imread function from the OpenCV library was used in grayscale mode to import images into a numpy array from a single folder containing TIFF images. The array was then exported as a single TIFF stack into a temporary folder using the mimwrite function from the imageio library, and the process was repeated for each folder. The NoRMCorre algorithm (Pnevmatikakis & Giovannucci, 2017) embedded in the CaImAn library (Giovannucci et al., 2019) was used to apply motion correction to each of the TIFF files. The data were then imported into a numpy array, rounded, and converted to 16-bit integers. The images were filtered using a 2D Gaussian filter with a sigma value of 1 (Surface View) / 2 (Prism View) in each direction, then a 1D Gaussian temporal filter with a sigma value of 2 was applied using the ndimage.gaussian_filter and ndimage.gaussian_filter1d function from the scipy library, respectively.

Data Extraction: The ROI sets, which were manually created using ImageJ, were imported using the read_roi_zip function from the read_roi library. The sets were then used to create two

masks; one mask was used as a replica of the ROIs and the second mask was made around the original ROI (roughly four times larger in area). The smaller mask was applied to find the average pixel value within each ROI, while the larger mask was applied to find the average pixel value of the neuropil. The neuropil correction was applied using the following equation (Akerboom et al., 2012);

$$\text{Corrected value} = \text{Date value} - (0.4\ \text{X Neuropil value})$$

Δf/f values were then calculated by using the following equation.

$$\frac{\Delta \mathrm{f}}{\mathrm{f}} = \frac{(\text{Date value} - \text{Background value})}{\text{Background value}}$$

where the background value is the slope estimating the background levels with fluorescence bleaching factored in. The data were then reorganized so that all segments with the same stimulus frequency and stimulus amplitude were grouped together.

Cell Flagging: The correlation coefficient between each of the trials was calculated using the stats. Pearsonr function from the scipy library. The average correlation coefficient was calculated for each stimulus frequency and stimulus amplitude. Similar to previous work(Wong & Borst, 2019), if the average correlation coefficient was above the threshold of 0.6, the cell was flagged as being responsive to that stimulus combination of frequency and amplitude, and the best frequency and characteristic frequency were calculated for the cell (Barnstedt et al., 2015).

Tonotopic Map Generation: The average radius for all ROIs were calculated to ensure that all cells on the tonotopic map will have uniform radii. A color key was also generated, with each shade of green representing one frequency. A blank canvas was generated using the Image module from the pillow library, and a circle was created for each cell and filled with the shade of green that represents the cell's best frequency or characteristic frequency, depending on the map. Cells that were non-responsive to stimuli were filled in red. The statistics for the data set,

such as the total number of cells, number of responsive cells, and number of non-responsive cells were tallied up and exported in an Excel spreadsheet.

Statistics:

All statistical analysis and the graphs (Figure 6) were made using Origin Pro 2022 software. The normality of the distributions of the data was examined using a Kolmogorov-Smirnov test. Accordingly, the proper statistical test was used. Chi-square test was used for categorical analysis and two-samples Kolmogorov-Smirnov Test was used examining the difference in data distribution. The cumulative frequency function was computed to calculate the fraction of cells tuned at each frequency based on their best frequency. Differences were deemed significant when p-value <0.05.

Histology:

After the 2P imaging, the mouse was transcardially perfused with 4% paraformaldehyde (PFA) solution in PBS solution. The isolated brain was then placed overnight in PFA for a complete fixation. The brain was then moved from the PFA to a graded sucrose solution (10, 20, and 30%) until it sunk. 50 μm coronal sections were taken at the level of the IC using a Leica cryostat. The sections were then mounted on a slide, coverslipped, and imaged using an epifluorescence microscope for imaging the GFP signals as an indicator for the GABAergic cells in the GAD67-GFP knock-in mouse (excitation: 488 nm and emissions: 515–550 nm).

Artwork:

The cartoon of mouse brain in figures 1 C, F and I was obtained from Brain Explorer 3D viewer Allen Mouse Brain (https://connectivity.brain-map.org/3d-viewer?v=1) and modified to be suitable for illustration. All figures were designed and made using Adobe Illustrator (Adobe, San Jose, CA). To keep working within Adobe environment to avoid losing the resolution of the

figures, Adobe Photoshop (Adobe, San Jose, CA) was used to crop the borders of some images to save space.

Acknowledgment

We thank Dr. Kush Paul (Bruker), Dr. Jason Maclean (The Department of Neurobiology, University of Chicago), and Dr. Michael Jacobs Goard (Neuroscience Research Institute, The University of California- Santa Barbara) for their valuable advice and guidance.

Competing interests

On behalf of all authors, there are no financial or non-financial competing interests to be declared.

References

Akerboom, J., Carreras Calderón, N., Tian, L., Wabnig, S., Prigge, M., Tolö, J., . . . Looger, L. L. (2013). Genetically encoded calcium indicators for multi-color neural activity imaging and combination with optogenetics. *Front Mol Neurosci, 6*, 2. doi:10.3389/fnmol.2013.00002

Akerboom, J., Chen, T. W., Wardill, T. J., Tian, L., Marvin, J. S., Mutlu, S., . . . Looger, L. L. (2012). Optimization of a GCaMP calcium indicator for neural activity imaging. *J Neurosci, 32*(40), 13819-13840. doi:10.1523/JNEUROSCI.2601-12.2012

Andermann, M. L., Gilfoy, N. B., Goldey, G. J., Sachdev, R. N., Wölfel, M., McCormick, D. A., . . . Levene, M. J. (2013). Chronic cellular imaging of entire cortical columns in awake mice using microprisms. *Neuron, 80*(4), 900-913. doi:10.1016/j.neuron.2013.07.052

Astl, J., Popelár, J., Kvasnák, E., & Syka, J. (1996). Comparison of response properties of neurons in the inferior colliculus of guinea pigs under different anesthetics. *Audiology, 35*(6), 335-345. doi:10.3109/00206099609071954

Bajo, V. M., & Moore, D. R. (2005). Descending projections from the auditory cortex to the inferior colliculus in the gerbil, Meriones unguiculatus. *J Comp Neurol, 486*(2), 101-116. doi:10.1002/cne.20542

Bal, U., Andresen, V., Baggett, B., & Utzinger, U. (2013). Intravital confocal and two-photon imaging of dual-color cells and extracellular matrix mimics. *Microsc Microanal, 19*(1), 201-212. doi:10.1017/S1431927612014080

Bandyopadhyay, S., Shamma, S. A., & Kanold, P. O. (2010). Dichotomy of functional organization in the mouse auditory cortex. *Nat Neurosci, 13*(3), 361-368. doi:10.1038/nn.2490

Barnstedt, O., Keating, P., Weissenberger, Y., King, A. J., & Dahmen, J. C. (2015). Functional Microarchitecture of the Mouse Dorsal Inferior Colliculus Revealed through In Vivo Two-Photon Calcium Imaging. *J Neurosci, 35*(31), 10927-10939. doi:10.1523/JNEUROSCI.0103-15.2015

Baumann, S., Griffiths, T. D., Sun, L., Petkov, C. I., Thiele, A., & Rees, A. (2011). Orthogonal representation of sound dimensions in the primate midbrain. *Nat Neurosci, 14*(4), 423-425. doi:10.1038/nn.2771

Beckmann, L., Zhang, X., Nadkarni, N. A., Cai, Z., Batra, A., Sullivan, D. P., . . . Zhang, H. F. (2019). Longitudinal deep-brain imaging in mouse using visible-light optical coherence tomography through chronic microprism cranial window. *Biomed Opt Express, 10*(10), 5235-5250. doi:10.1364/BOE.10.005235

Centonze, V. E., & White, J. G. (1998). Multiphoton excitation provides optical sections from deeper within scattering specimens than confocal imaging. *Biophys J, 75*(4), 2015-2024. doi:10.1016/S0006-3495(98)77643-X

Chen, C., Cheng, M., Ito, T., & Song, S. (2018). Neuronal Organization in the Inferior Colliculus Revisited with Cell-Type-Dependent Monosynaptic Tracing. *J Neurosci, 38*(13), 3318-3332. doi:10.1523/JNEUROSCI.2173-17.2018

Chen, C., & Song, S. (2019). Differential cell-type dependent brain state modulations of sensory representations in the non-lemniscal mouse inferior colliculus. *Commun Biol, 2*, 356. doi:10.1038/s42003-019-0602-4

Chen, J. L., Andermann, M. L., Keck, T., Xu, N. L., & Ziv, Y. (2013). Imaging neuronal populations in behaving rodents: paradigms for studying neural circuits underlying behavior in the mammalian cortex. *J Neurosci, 33*(45), 17631-17640. doi:10.1523/JNEUROSCI.3255-13.2013

Chernock, M. L., Larue, D. T., & Winer, J. A. (2004). A periodic network of neurochemical modules in the inferior colliculus. *Hear Res, 188*(1-2), 12-20. doi:10.1016/S0378-5955(03)00340-X

Chia, T. H., & Levene, M. J. (2009). Microprisms for in vivo multilayer cortical imaging. *J Neurophysiol, 102*(2), 1310-1314. doi:10.1152/jn.91208.2008

Coleman, J. R., & Clerici, W. J. (1987). Sources of projections to subdivisions of the inferior colliculus in the rat. *J Comp Neurol, 262*(2), 215-226. doi:10.1002/cne.902620204

Cramer, S. W., Carter, R. E., Aronson, J. D., Kodandaramaiah, S. B., Ebner, T. J., & Chen, C. C. (2021). Through the looking glass: A review of cranial window technology for optical access to the brain. *J Neurosci Methods, 354*, 109100. doi:10.1016/j.jneumeth.2021.109100

Dana, H., Novak, O., Guardado-Montesino, M., Fransen, J. W., Hu, A., Borghuis, B. G., . . . Svoboda, K. (2018). Thy1 transgenic mice expressing the red fluorescent calcium indicator jRGECO1a for neuronal population imaging in vivo. *PLoS One, 13*(10), e0205444. doi:10.1371/journal.pone.0205444

Dillingham, C. H., Gay, S. M., Behrooz, R., & Gabriele, M. L. (2017). Modular-extramodular organization in developing multisensory shell regions of the mouse inferior colliculus. *J Comp Neurol, 525*(17), 3742-3756. doi:10.1002/cne.24300

DL, Oliver. (2005). Neuronal organization in the inferior colliculus. In Winer JA & Schreiner CE (Eds.), *The inferior colliculus.* (pp. 69–114). New York: Springer.

Faye-Lund, H., & Osen, K. K. (1985). Anatomy of the inferior colliculus in rat. *Anat Embryol (Berl), 171*(1), 1-20. doi:10.1007/BF00319050

Giovannucci, A., Friedrich, J., Gunn, P., Kalfon, J., Brown, B. L., Koay, S. A., . . . Pnevmatikakis, E. A. (2019). CaImAn an open source tool for scalable calcium imaging data analysis. *Elife, 8*. doi:10.7554/eLife.38173

Goldey, G. J., Roumis, D. K., Glickfeld, L. L., Kerlin, A. M., Reid, R. C., Bonin, V., . . . Andermann, M. L. (2014). Removable cranial windows for long-term imaging in awake mice. *Nat Protoc, 9*(11), 2515-2538. doi:10.1038/nprot.2014.165

Heys, J. G., Rangarajan, K. V., & Dombeck, D. A. (2014). The functional micro-organization of grid cells revealed by cellular-resolution imaging. *Neuron, 84*(5), 1079-1090. doi:10.1016/j.neuron.2014.10.048

Holtmaat, A., Bonhoeffer, T., Chow, D. K., Chuckowree, J., De Paola, V., Hofer, S. B., . . . Wilbrecht, L. (2009). Long-term, high-resolution imaging in the mouse neocortex through a chronic cranial window. *Nat Protoc, 4*(8), 1128-1144. doi:10.1038/nprot.2009.89

Horton, N. G., Wang, K., Kobat, D., Clark, C. G., Wise, F. W., Schaffer, C. B., & Xu, C. (2013). three-photon microscopy of subcortical structures within an intact mouse brain. *Nat Photonics, 7*(3). doi:10.1038/nphoton.2012.336

Ito, T., Hirose, J., Murase, K., & Ikeda, H. (2014). Determining auditory-evoked activities from multiple cells in layer 1 of the dorsal cortex of the inferior colliculus of mice by in vivo calcium imaging. *Brain Res, 1590*, 45-55. doi:10.1016/j.brainres.2014.09.049

Ito, T., & Oliver, D. L. (2012). The basic circuit of the IC: tectothalamic neurons with different patterns of synaptic organization send different messages to the thalamus. *Front Neural Circuits, 6*, 48. doi:10.3389/fncir.2012.00048

Jain, R., & Shore, S. (2006). External inferior colliculus integrates trigeminal and acoustic information: unit responses to trigeminal nucleus and acoustic stimulation in the guinea pig. *Neurosci Lett, 395*(1), 71-75. doi:10.1016/j.neulet.2005.10.077

JF, Willott. (2001). Handbook of mouse auditory research. In Willott JF (Ed.), *Behavior to molecular biology*. Boca Raton, FL: CRC.

Lamb-Echegaray, I. D., Noftz, W. A., Stinson, J. P. C., & Gabriele, M. L. (2019). Shaping of discrete auditory inputs to extramodular zones of the lateral cortex of the inferior colliculus. *Brain Struct Funct, 224*(9), 3353-3371. doi:10.1007/s00429-019-01979-6

Lesicko, A. M. H., Sons, S. K., & Llano, D. A. (2020). Circuit Mechanisms Underlying the Segregation and Integration of Parallel Processing Streams in the Inferior Colliculus. *J Neurosci, 40*(33), 6328-6344. doi:10.1523/JNEUROSCI.0646-20.2020

Lesicko, A. M., Hristova, T. S., Maigler, K. C., & Llano, D. A. (2016). Connectional Modularity of Top-Down and Bottom-Up Multimodal Inputs to the Lateral Cortex of the Mouse Inferior Colliculus. *J Neurosci, 36*(43), 11037-11050. doi:10.1523/JNEUROSCI.4134-15.2016

Loftus, W. C., Malmierca, M. S., Bishop, D. C., & Oliver, D. L. (2008). The cytoarchitecture of the inferior colliculus revisited: a common organization of the lateral cortex in rat and cat. *Neuroscience, 154*(1), 196-205. doi:10.1016/j.neuroscience.2008.01.019

Low, R. J., Gu, Y., & Tank, D. W. (2014). Cellular resolution optical access to brain regions in fissures: imaging medial prefrontal cortex and grid cells in entorhinal cortex. *Proc Natl Acad Sci U S A, 111*(52), 18739-18744. doi:10.1073/pnas.1421753111

Marks, T. D., & Goard, M. J. (2021). Stimulus-dependent representational drift in primary visual cortex. *Nat Commun, 12*(1), 5169. doi:10.1038/s41467-021-25436-3

Ouzounov, D. G., Wang, T., Wang, M., Feng, D. D., Horton, N. G., Cruz-Hernández, J. C., . . . Xu, C. (2017). In vivo three-photon imaging of activity of GCaMP6-labeled neurons deep in intact mouse brain. *Nat Methods, 14*(4), 388-390. doi:10.1038/nmeth.4183

Pnevmatikakis, E. A., & Giovannucci, A. (2017). NoRMCorre: An online algorithm for piecewise rigid motion correction of calcium imaging data. *J Neurosci Methods, 291*, 83-94. doi:10.1016/j.jneumeth.2017.07.031

Redman, W. T., Wolcott, N. S., Montelisciani, L., Luna, G., Marks, T. D., Sit, K. K., . . . Goard, M. J. (2022). Long-term transverse imaging of the hippocampus with glass microperiscopes. *Elife, 11*. doi:10.7554/eLife.75391

Romand, R., & Ehret, G. (1990). Development of tonotopy in the inferior colliculus. I. Electrophysiological mapping in house mice. *Brain Res Dev Brain Res, 54*(2), 221-234. doi:10.1016/0165-3806(90)90145-o

Romero, S., Hight, A. E., Clayton, K. K., Resnik, J., Williamson, R. S., Hancock, K. E., & Polley, D. B. (2020). Cellular and Widefield Imaging of Sound Frequency Organization in Primary and Higher Order Fields of the Mouse Auditory Cortex. *Cereb Cortex, 30*(3), 1603-1622. doi:10.1093/cercor/bhz190

Rothschild, G., Nelken, I., & Mizrahi, A. (2010). Functional organization and population dynamics in the mouse primary auditory cortex. *Nat Neurosci, 13*(3), 353-360. doi:10.1038/nn.2484

Saldaña, E., Feliciano, M., & Mugnaini, E. (1996). Distribution of descending projections from primary auditory neocortex to inferior colliculus mimics the topography of intracollicular projections. *J Comp Neurol, 371*(1), 15-40. doi:10.1002/(SICI)1096-9861(19960715)371:1<15::AID-CNE2>3.0.CO;2-O

Schreiner, C. E., & Langner, G. (1988). Periodicity coding in the inferior colliculus of the cat. II. Topographical organization. *J Neurophysiol, 60*(6), 1823-1840. doi:10.1152/jn.1988.60.6.1823

Schreiner, Christoph E, & Winer, Jeffery A. (2005). *The inferior colliculus*: Springer Science+ Business Media, Incorporated.

Stiebler, I., & Ehret, G. (1985). Inferior colliculus of the house mouse. I. A quantitative study of tonotopic organization, frequency representation, and tone-threshold distribution. *J Comp Neurol, 238*(1), 65-76. doi:10.1002/cne.902380106

Tamamaki, N., Yanagawa, Y., Tomioka, R., Miyazaki, J., Obata, K., & Kaneko, T. (2003). Green fluorescent protein expression and colocalization with calretinin, parvalbumin, and somatostatin in the GAD67-GFP knock-in mouse. *J Comp Neurol, 467*(1), 60-79. doi:10.1002/cne.10905

Ter-Mikaelian, M., Sanes, D. H., & Semple, M. N. (2007). Transformation of temporal properties between auditory midbrain and cortex in the awake Mongolian gerbil. *J Neurosci, 27*(23), 6091-6102. doi:10.1523/JNEUROSCI.4848-06.2007

Wenzel, M., Hamm, J. P., Peterka, D. S., & Yuste, R. (2017). Reliable and Elastic Propagation of Cortical Seizures In Vivo. *Cell Rep, 19*(13), 2681-2693. doi:10.1016/j.celrep.2017.05.090

Willard FH, & DK, Ryugo. (1983). Anatomy of the central auditory system. In Willott JF (Ed.), *The auditory psychobiology of the mouse.* (pp. 201-304). Springfield, IL: Thomas.

Winer, J. A., Larue, D. T., Diehl, J. J., & Hefti, B. J. (1998). Auditory cortical projections to the cat inferior colliculus. *J Comp Neurol, 400*(2), 147-174.

Wong, A. B., & Borst, J. G. G. (2019). Tonotopic and non-auditory organization of the mouse dorsal inferior colliculus revealed by two-photon imaging. *Elife, 8*. doi:10.7554/eLife.49091

Xiong, B., Li, A., Lou, Y., Chen, S., Long, B., Peng, J., . . . Gong, H. (2017). Precise Cerebral Vascular Atlas in Stereotaxic Coordinates of Whole Mouse Brain. *Front Neuroanat, 11*, 128. doi:10.3389/fnana.2017.00128

Yang, W., & Yuste, R. (2017). In vivo imaging of neural activity. *Nat Methods, 14*(4), 349-359. doi:10.1038/nmeth.4230

Zhou, J., & Shore, S. (2006). Convergence of spinal trigeminal and cochlear nucleus projections in the inferior colliculus of the guinea pig. *J Comp Neurol, 495*(1), 100-112. doi:10.1002/cne.20863